

Magnon-magnon coupling in noncollinear synthetic antiferromagnets

Tengfei Zhang(张腾飞), Quwen Wang(王曲文), Min Chen(陈敏), Jie Dong(董洁), Qian Zhao(赵乾), Zimu Li(李子木), Qingfang Liu(刘青芳), Jianbo Wang(王建波), and Jinwu Wei(魏晋武)
Citation : Chin. Phys. B, 2025, 34 (**5**): 057201. DOI: 10.1088/1674-1056/adb26b
http://cpb.iphy.ac.cn; http://iopscience.iop.org/cpb

What follows is a list of articles you may be interested in

Controlled crossover of electron transport in graphene nanoconstriction: From Coulomb blockade to electron interference

Wei Yu(余炜), Xiao Guo(郭潇), Yuwen Cai(蔡煜文), Xiaotian Yu(俞晓天), and Wenjie Liang(梁文杰)
Chin. Phys. B, 2023, 32 (**7**): 077202. DOI: 10.1088/1674-1056/accf67

Tunable valley filter efficiency by spin-orbit coupling in silicene nanoconstrictions

Yi-Jian Shi(施一剑), Yuan-Chun Wang(王园春), and Peng-Jun Wang(汪鹏君)
Chin. Phys. B, 2021, 30 (**5**): 057201. DOI: 10.1088/1674-1056/abcf35

Role of Ag microalloying on glass forming ability and crystallization kinetics of ZrCoAgAlNi amorphous alloy

A Surendar, K Geetha, C Rajan, and M Alaazim
Chin. Phys. B, 2021, 30 (**1**): 017201. DOI: 10.1088/1674-1056/abb65e

Spin Seebeck effect and spin Hall magnetoresistance in the Pt/$Y_3Fe_5O_{12}$ heterostructure under laser-heating

Shuanhu Wang(王拴虎), Gang Li(李刚), Jianyuan Wang(王建元), Yingyi Tian(田颖异), Hongrui Zhang(张洪瑞), Lvkuan Zou(邹吕宽), Jirong Sun(孙继荣), Kexin Jin(金克新)
Chin. Phys. B, 2018, 27 (**11**): 117201. DOI: 10.1088/1674-1056/27/11/117201

Direct spin-phonon coupling of spin-flip relaxation in quantum dots

Ji-Wen Yin(尹辑文), Wei-Ping Li(李伟萍), Hong-Juan Li(李红娟), Yi-Fu Yu(于毅夫)
Chin. Phys. B, 2017, 26 (**1**): 017201. DOI: 10.1088/1674-1056/26/1/017201

SPECIAL TOPIC — Advanced magnonics

Magnon–magnon coupling in noncollinear synthetic antiferromagnets

Tengfei Zhang(张腾飞)[1], Quwen Wang(王曲文)[1], Min Chen(陈敏)[2], Jie Dong(董洁)[1], Qian Zhao(赵乾)[1], Zimu Li(李子木)[1], Qingfang Liu(刘青芳)[1], Jianbo Wang(王建波)[1], and Jinwu Wei(魏晋武)[1,†]

[1] *School of Physical Science and Technology, Lanzhou University, Lanzhou* 730000, *China*
[2] *Southwest Institute of Applied Magnetics, Mianyang* 621000, *China*

(Received 10 December 2024; revised manuscript received 16 January 2025; accepted manuscript online 5 February 2025)

We report a theoretical analysis of magnon–magnon coupling in a noncollinear magnetic sandwiched structure with interlayer exchange interaction, which consists of two ferromagnetic layers with perpendicular and in-plane magnetic anisotropy, respectively. Based on the Landau–Lifshitz equation, the spin wave dispersion is derived, and then the frequency gap is observed due to the magnon–magnon coupling effect induced by symmetry breaking. The influence of saturation magnetization, exchange coupling interaction, perpendicular magnetic anisotropy, and wave vector on the coupling strength is studied in detail. We find that the coupling strength is strongly dependent on the saturation magnetization and a small saturation magnetization can lead to strong coupling strength. By selecting the appropriate magnetic materials, the ultra-strong coupling regime can be achieved. The precession information in time domain is solved and the alternating change of the precession components in two ferromagnetic layers implies the exchange of energy and information.

Keywords: magnon–magnon coupling, noncollinear magnetic structure, coupling strength

PACS: 72.10.Di, 75.50.Ee, 72.10.Di

DOI: 10.1088/1674-1056/adb26b **CSTR:** 32038.14.CPB.adb26b

Magnons, the quantization of collective spin excitations in ferromagnets, have attracted extensive attention in both fundamental and applied research fields and given birth to magnonics.[1–6] Magnonics addresses the physical properties of magnons and utilizes them to process information[7–10] or build the hybrid quantum systems.[11–16] For the hybridization of magnons with a quantum system, the reading and control of qubits can be achieved by coupling in the magnonics cavity, which has smaller volume and lower Ohmic losses than the microwave cavity.[17–19] In order to improve the performances and facilitate the development of the magnon-based functional quantum devices, it is vital to enhance the strength of coupling. Recently, the strong magnon–magnon coupling has been reported in magnetic nanostructures and multilayers,[20,21] which can be analogous to the hybrid quantum system. It is found that the strength of magnon–magnon coupling can be enhanced due to the stronger intralayer exchange coupling in a ferrimagnetic gadolinium iron garnet, approaching 6.38 GHz.[17] Moreover, magnon–magnon coupling due to the interlayer exchange interaction has also been demonstrated in a layered antiferromagnet $CrCl_3$ and in synthetic antiferromagnets (SAFs), in which the coupling between acoustic mode (AM) and optic mode (OM) was excited.[22] Among these, due to the adjustable exchange coupling (AEC) between two ferromagnetic layers and the breaking of magnetic symmetry,[23] the popularity of synthetic antiferromagnets (SAFs) has increased as they can break symmetry through spin pumping and the external magnetic field component, among other advantages. This is beneficial for controlling the coupling strength, which is conducive to controlling the coupling strength. The magnon–magnon coupling effect has been observed in the in-plane SAFs (CoFeB/Ru/CoFeB and NiFe/Ru/NiFe multilayers) and in perpendicularly magnetized SAFs (MgO/CoFeB/W/CoFeB/MgO structures).[24–28]

From a physical picture viewpoint, the key to realize a strong and tunable magnon–magnon coupling in SAF is to break the parity symmetry. A simple approach is to employ an external magnetic field tilted toward the out-of-plane direction.[29–32] Recent reports[33] show that the perpendicularly magnetized SAFs have ultra-strong magnon–magnon coupling when an external magnetic field is applied perpendicular to the direction of Néel vector. In particular, the magnon–magnon coupling occurs when the magnetization of two FM layers in SAF forms a T-type configuration, namely, the magnetization in one FM layer tends to in-plane while the other remains in the out-of-plane direction. To date, the in-plane and out-of-plane SAF structures have been extensively researched and an external magnetic field is employed to break the parity symmetry. Natural noncollinear antiferromagnets have been extensively studied.[34–36] However, the noncollinear SAFs,

†Corresponding author. E-mail: weijw@lzu.edu.cn

© 2025 Chinese Physical Society and IOP Publishing Ltd. All rights, including for text and data mining, AI training, and similar technologies, are reserved.

such as natural T-type, are rarely studied, which have intrinsic symmetry-breaking.

In this paper, we theoretically study the magnon–magnon coupling in noncollinear SAFs, namely, a T-type magnetic structure with interlayer exchange interaction. Acoustic and optical modes are observed and coupled due to symmetry breaking. Considering the different physical parameters in the noncollinear magnetic structure, including the saturation magnetization, perpendicular magnetic anisotropy, interlayer exchange interaction, dynamical dipolar interaction, we systematically study the coupling strength based on the Landau–Lifshitz equation.

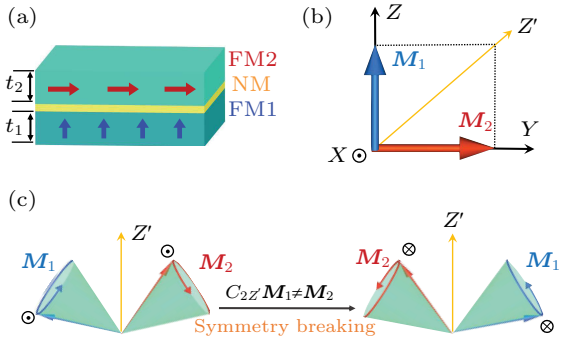


Fig. 1. Structure and symmetry breaking in noncollinear SAFs. (a) Schematic diagram of a magnetic multilayer with noncollinear mangetization, and the blue (red) arrows represent the magnetization in FM1(2) with perpendicular (in-plane) magnetic anisotropy, NM is the non-magnetic spacer layer. (b) The macrospin equilibrium state of FM1 and FM2 in a XYZ-coordinate with $\boldsymbol{M}_1$ along the Z axis and $\boldsymbol{M}_2$ along the Y axis. The orange arrow represents the direction of rotational axis, $\boldsymbol{Z}' \parallel (\boldsymbol{M}_1 + \boldsymbol{M}_2)$. (c) Sketch of symmetry breaking. A rotational symmetry operation $C_{2Z'}$ along the Z' axis is applied and $C_{2Z'}\boldsymbol{M}_1 \neq \boldsymbol{M}_2$.

Figure 1(a) shows the sample structure with noncollinear magnetic configuration, in which the FM layer 1 with thickness t_1 and saturation magnetization M_{s1} has perpendicular magnetic anisotropy (PMA) and the FM layer 2 with thickness t_2 and saturation magnetization M_{s2} has an in-plane magnetic anisotropy. These two FM layers form ferromagnetic or antiferromagnetic (AFM) coupling through the interlayer Ruderman–Kittel–Kasuya–Yoshida (RKKY) interaction mediated by a sandwiched spacer layer. In this noncollinear magnetic structure, the intrinsic symmetry breaking will induce a strong magnon–magnon coupling. In the absence of an external magnetic field, a XYZ coordinate is set along the magnetization, as shown in Fig. 1(b), where $\boldsymbol{M}_1$ and $\boldsymbol{M}_2$ are parallel to the Z and Y axes, respectively. The rotational axis is established by $\boldsymbol{Z}' \parallel (\boldsymbol{M}_1 + \boldsymbol{M}_2)$. We define a rotation operator $C_{2Z'}$, which can rotate the magnetic vector around the Z' axis by 180° and obviously $C_{2Z'}^2 = 1$. When interlayer exchange coupling is absent, we can obtain $C_{2Z'}\boldsymbol{M}_1 = \boldsymbol{M}_2$. However, when interlayer coupling exists and $\boldsymbol{H}_{\rm ext} \parallel \hat{e}_Y$, the magnetization of the two ferromagnetic layers deviates from the easy axis and forms an angle with the film plane and $C_{2Z'}\boldsymbol{M}_1 \neq \boldsymbol{M}_2$, thus structures with intrinsic symmetry breaking are present in interlayer-coupled noncollinear synthetic antiferromagnets. In addition, because the two FM layers have different saturation magnetization and magnetic anisotropy, the operation $C_{2Z'}$ on $\boldsymbol{M}_1$ ($\boldsymbol{M}_2$) is not equal to the vector $\boldsymbol{M}_2$ ($\boldsymbol{M}_1$), as shown in Fig. 1(c). This intrinsic symmetry breaking in noncollinear magnetic structure thus induces the magnon–magnon coupling between acoustic and optic modes.

Based on the Landau–Lifshitz (LL) equation and the total energy density of the magnetic system, we have carried out the macrospin simulation. Figure 2(a) shows two Cartesian coordinates in a noncollinear T-type magnetic structure, including a fixed coordinate frame XYZ and a dynamic coordinate frame xyz, where the Z axis is perpendicular to the magnetic film and the Y axis is parallel to the external magnetic field $\boldsymbol{H}_{\rm ext}$, the z axis is along the magnetization at the equilibrium state; the axes x and X coincide with each other. On the basis of the Stoner–Wohlfarth model, the macrospin simulation is performed. In coordinate XYZ, the total energy density of this noncollinear SAF can be expressed as

$$\begin{aligned}\varepsilon_{\rm tot} =& -\sum\nolimits_{i=1,2}\mu_0 M_{{\rm s},i}t_i H_{\rm ext}\sin\theta_i \\ &-\left[\left(t_1K_1-\frac{\mu_0 M_{\rm s1}^2 t_1}{2}\right)\cdot(\hat{m}_1\cdot\hat{e}_Z)^2\right. \\ &\left.-\frac{1}{2}\mu_0 H_{\rm k2}M_{\rm S}t_2\cdot(\hat{m}_2\cdot\hat{e}_Z)^2\right]+J_{\rm ex}\boldsymbol{m}_1\cdot\boldsymbol{m}_2, \end{aligned} \tag{1}$$

where the first term is the Zeeman energy, the second term is the magnetic anisotropy energy, and the third term is the interlayer exchange coupling energy. θ_i is the polar angle between the Z axis and the magnetization of FM layer i (1, 2). $H_{\rm ext}$ is an external magnetic field along the Y axis. K_1 is the perpendicular anisotropy energy of FM1. The negative value of $H_{\rm k2}$ is used to characterize the intensity of the easy plane anisotropy. The $J_{\rm ex}$ is the exchange energy density per unit area, which is a negative (positive) value for the FM (AFM) coupling. The effective fields acting on the magnetization can be thus obtained by

$$\boldsymbol{H}_i = -\nabla_{\boldsymbol{m}_i}\left(\frac{\varepsilon_{\rm tot}}{\mu_0 M_{{\rm s},i}t_i}\right)+\boldsymbol{h}_{{\rm dip},i}.$$

Therefore, the LL equation can be expressed as

$$\frac{{\rm d}\boldsymbol{M}_i}{{\rm d}t} = -\gamma\boldsymbol{M}_i\times\boldsymbol{H}_i, \tag{2}$$

$$\begin{aligned}\boldsymbol{H}_1 =& H_{\rm ext}\hat{e}_y + H_{\rm k1}(\hat{m}_1\cdot\hat{e}_z)\hat{e}_z \\ &+H_{\rm ex1}\hat{m}_2+\boldsymbol{h}_{{\rm dip},1}, \end{aligned} \tag{3a}$$

$$\begin{aligned}\boldsymbol{H}_2 =& H_{\rm ext}\hat{e}_y - M_{\rm s2}(\hat{m}_2\cdot\hat{e}_z)\hat{e}_z \\ &+H_{\rm ex2}\hat{m}_1+\boldsymbol{h}_{{\rm dip},2}, \end{aligned} \tag{3b}$$

where γ is the gyromagnetic ratio. $H_{\rm k1} = 2K_1/M_{\rm s1}$ is the effective perpendicular anisotropy field, $H_{{\rm ex},i} = J_{\rm ex}/(\mu_0 t_i M_{si})$ is the effective field of RKKY exchange interaction acting on the FM layer i, and the type of interlayer coupling can be determined by the positive or negative sign of $J_{\rm ex}$. $\boldsymbol{h}_{{\rm dip},i}$ is the effective

field of dynamic dipole interaction. The detailed expressions of effective fields $\boldsymbol{H}_i$ are given in Appendix A.

In order to reduce the number of variables, numerical calculation will be carried out in the dynamic coordinate frame *xyz*. The effective fields need to be transformed from the fixed *XYZ* coordinate to the moving *xyz* coordinate through a rotation matrix $R_x(\theta)$, as shown by the following expression:

$$\begin{pmatrix} x \\ y \\ z \end{pmatrix} = \begin{pmatrix} 1 & 0 & 0 \\ 0 & \cos\theta & -\sin\theta \\ 0 & \sin\theta & \cos\theta \end{pmatrix} \begin{pmatrix} X \\ Y \\ Z \end{pmatrix}. \tag{4}$$

In the *xyz* coordinate, the magnetization and effective field in FM layer *i* can be expressed as

$$\boldsymbol{m}_{\mathrm{eff},i}(x,t) = R_x(\theta_i)\boldsymbol{M}_i = \begin{pmatrix} m_{xi}\,\mathrm{e}^{\mathrm{i}(kx+\omega t)} \\ m_{yi}\,\mathrm{e}^{\mathrm{i}(kx+\omega t)} \\ 1 \end{pmatrix}, \tag{5}$$

$$\begin{aligned} \boldsymbol{H}_{\mathrm{eff},i} &= R_x(\theta_i)\boldsymbol{H}_i + R_x(\theta_i)\boldsymbol{h}_{\mathrm{dip},i} \\ &= \begin{pmatrix} H^x_{\mathrm{eff},i} \\ H^y_{\mathrm{eff},i} \\ H^z_{\mathrm{eff},i} \end{pmatrix} + R_x(\theta_i) \begin{pmatrix} h^x_{\mathrm{dip},i} \\ h^y_{\mathrm{dip},i} \\ h^z_{\mathrm{dip},i} \end{pmatrix}. \end{aligned} \tag{6}$$

Here, dynamic dipole fields acting on the FM layer with in-plane magnetic anisotropy[37,38] or PMA[39,40] can be obtained through the microscopic Maxwell equation[39]

$$\begin{cases} \nabla\cdot(\boldsymbol{h}_{\mathrm{d}} + 4\pi M_{\mathrm{S}}\boldsymbol{m}) = 0, \\ \nabla\times\boldsymbol{h}_{\mathrm{d}} = 0. \end{cases} \tag{7}$$

In noncollinear synthetic antiferromagnets, the boundary conditions of in-plane ferromagnetic layer (IP-FM) and perpendicularly magnetized ferromagnetic layer (PMA-FM) are different. Assuming that the form of the dipole field of IP-FM (PMA-FM) is consistent with that of the collinear SAF,[37] the dynamic dipole field of IP-FM (PMA-FM) is consistent with the dynamic dipole field of IP-SAF (PMA-SAF). The dynamic dipole fields in noncollinear SAF can be represented by two parts:

$$\begin{aligned} \boldsymbol{h}_{\mathrm{dip},1} &= \boldsymbol{h}^{\mathrm{PMA}}_{\mathrm{self-dip}} + \boldsymbol{h}^{\mathrm{IP}}_{\mathrm{mutual-dip}} \\ &= -2\pi k t_1 \begin{pmatrix} m_{x1} \\ 0 \\ 0 \end{pmatrix} - 2\pi k t_2 \begin{pmatrix} m_{x2} - \mathrm{i}m_{y2} \\ 0 \\ -\mathrm{i}m_{x2} - m_{y2} \end{pmatrix}, \end{aligned} \tag{8}$$

$$\begin{aligned} \boldsymbol{h}_{\mathrm{dip},2} &= \boldsymbol{h}^{\mathrm{IP}}_{\mathrm{self-dip}} + \boldsymbol{h}^{\mathrm{PMA}}_{\mathrm{mutual-dip}} \\ &= -2\pi k t_2 \begin{pmatrix} m_{x2} \\ 0 \\ -m_{y2} \end{pmatrix} - 2\pi k t_1 \begin{pmatrix} m_{x1} \\ 0 \\ \mathrm{i}m_{x1} \end{pmatrix}, \end{aligned} \tag{9}$$

where $\boldsymbol{h}^{\mathrm{PMA}}_{\mathrm{self-dip}}$ and $\boldsymbol{h}^{\mathrm{IP}}_{\mathrm{self-dip}}$ represent the intralayer dipole fields in the FM with PMA and in-plane magnetic anisotropy, respectively. $\boldsymbol{h}^{\mathrm{IP}}_{\mathrm{mutual-dip}}$ and $\boldsymbol{h}^{\mathrm{PMA}}_{\mathrm{mutual-dip}}$ denote the interlayer dipole fields generated from the FM with in-plane magnetic anisotropy and PMA, respectively. k is the wave vector of spin wave, which can be experimentally determined through the incident angle of laser beam in Brillouin light scattering or the geometric structure of microwave antenna. We have studied the magnetostatic surface spin wave (MSSW) mode, that is, the wave vector k propagates in the positive direction along the X-axis.

The spin wave dispersion relation in noncollinear SAF can be thus obtained by solving Eqs. (2) and (3). When the magnetization deviates from the equilibrium position and experiences the Larmor precession with a small angle, the LL equations can be simplified to

$$\begin{pmatrix} \mathrm{i}\omega/\gamma & A_{12} & A_{13} & A_{14} \\ A_{21} & \mathrm{i}\omega/\gamma & A_{23} & A_{24} \\ A_{31} & A_{32} & \mathrm{i}\omega/\gamma & A_{34} \\ A_{41} & A_{42} & A_{43} & \mathrm{i}\omega/\gamma \end{pmatrix} \begin{pmatrix} m_{x1} \\ m_{y1} \\ m_{x2} \\ m_{y2} \end{pmatrix} = 0. \tag{10}$$

Where the elements of coefficient matrix are listed in Appendix A. As a result, the analytical expression of the resonance frequency $f = \omega/2\pi$ can be obtained by calculating the eigenvalue of the coefficient matrix. The result indicates that the intrinsic spin wave dispersion of the noncollinear magnetic structure is dependent on the saturation magnetizations of two FM layers (M_{s1} and M_{s2}), perpendicular magnetic anisotropy (H_{k1}), interlayer exchange interaction (J_{ex}), and spin wave vector (k). In order to simplify the calculations, the dispersion relation can be obtained through the numerical computation method, which is used to produce and explain the following results.

Now, let us discuss the equilibrium state of the noncollinear magnetic structure. When an external magnetic field is applied along the positive direction of the Y axis, the total energy, including Zeeman energy, perpendicular magnetic anisotropy energy and interlayer exchange energy, is considered. According to the principle of free energy minimization, the equilibrium position of macrospin $\boldsymbol{M}_{1(2)}$ can be determined by the differential method, namely, $\partial\varepsilon_{\mathrm{tot}}/\partial\theta_1 = 0$ and $\partial\varepsilon_{\mathrm{tot}}/\partial\theta_2 = 0$. Figures 2(b)–2(d) show the magnetic field dependence of the angle $\theta_{1(2)}$ of magnetization $\boldsymbol{M}_{1(2)}$ deviating from the Z axis. When the interlayer RKKY exchange interaction is zero, namely, the two FM layers have no coupling, the magnetization $\boldsymbol{M}_1$ and $\boldsymbol{M}_2$ are perpendicular to each other and form a standard T-shaped structure at zero magnetic field, as shown in Fig. 2(b). With the increase of external magnetic field, the $\boldsymbol{M}_1$ gradually deviates to the Y axis and $\boldsymbol{M}_2$ remains unchanged. When the magnetic field increases to 5 kOe, the $\boldsymbol{M}_1$ and $\boldsymbol{M}_2$ are arranged in parallel along the Y direction. Here the PMA of FM layer 1 is set to 5 kOe, and the saturation magnetization of two FM layers are set to the same 1300 emu/cm^3. When the type of interlayer exchange coupling is FM coupling and the $J_{\mathrm{ex}} = -0.1$ erg/cm^2, the $\boldsymbol{M}_1$ and $\boldsymbol{M}_2$ tend to be arranged in parallel at zero magnetic field, as shown in Fig. 2(c), in which the $\boldsymbol{M}_1$ deviates from the X axis clockwise and the $\boldsymbol{M}_2$ deviates from the Y axis counterclockwise. When the type of interlayer exchange coupling is

antiferromagnetic coupling and $J_{ex} = +0.1$ erg/cm^2, as shown in Fig. 2(d), the RKKY exchange interaction makes $\boldsymbol{M}_1$ and $\boldsymbol{M}_2$ tend to be antiparallel at zero magnetic field, and the $\boldsymbol{M}_1$ deviates from the X axis counter-clockwise, $\boldsymbol{M}_2$ deviates from the Y axis clockwise. For the above three cases of no coupling, FM and AFM coupling, the $\boldsymbol{M}_1$ and $\boldsymbol{M}_2$ gradually turn to the direction of the Y axis with the increase of external magnetic field, and they are parallel with the Y axis when the magnetic field reaches 5 kOe. When considering the interlayer RKKY exchange interaction, the $\boldsymbol{M}_1$ ($\boldsymbol{M}_2$) deviates from the Z (Y) axis with a small angle at the absence of magnetic field. The deviation angle is related to the magnitude and type of interlayer exchange coupling, which also affects magnon–magnon coupling.

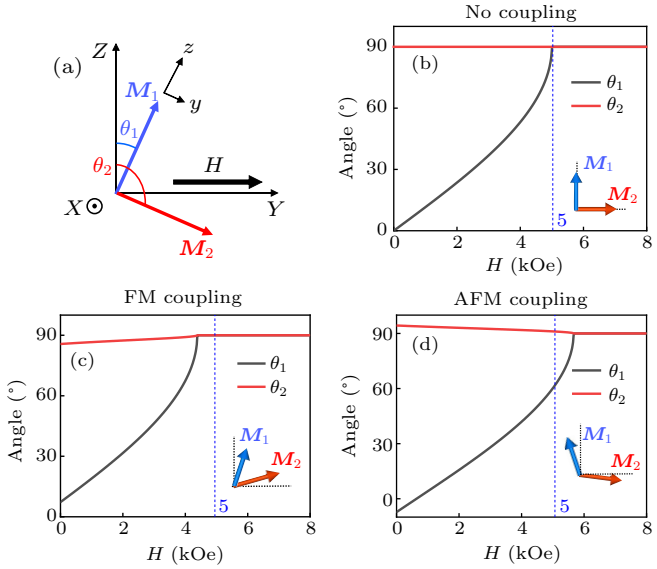


Fig. 2. Equilibrium state of H_{ext} and the coordinate system. (a) A fixed XYZ-coordinate and two motional xyz-coordinates. The macrospin $\boldsymbol{M}_1$ and $\boldsymbol{M}_2$ are in the ZY plane and $\theta_{1(2)}$ is the polar angle between the Z axis and $\boldsymbol{M}_{1(2)}$. The motional z axis is along the equilibrium direction of $\boldsymbol{M}_1$ and $\boldsymbol{M}_2$, and the motional x axis is parallel to the fixed X axis. The external magnetic field is along the Y axis, and the spin wave vector is along the X axis. (b)–(d) The magnetic field dependent of $\theta_{1(2)}$ at the equilibrium state when the interlayer exchange energy $J_{ex} = 0$ (no coupling), $J_{ex} < 0$ (FM coupling), and $J_{ex} > 0$ (AFM coupling), respectively. The blue dashed line is the reference line for $H_{ext} = 5$ kOe.

At equilibrium state, the intrinsic dispersion relation of noncollinear magnetic structure can be determined by Eq. (10). When a small alternating magnetic field with frequency $f = \omega/2\pi$ acts on the magnetizations, they will deviate from the equilibrium position and precess at a small angle. The inconsistent precession in magnetic sample produces spin waves via direct exchange interaction and dynamical dipole interaction. In our case, spin wave propagates along the direction of the X axis. Figure 3(a) shows the typical dispersion relation of spin wave in a T-type magnetic structure. Here the parameters are $M_{s1} = M_{s2} = 1300$ emu/cm^3, $H_{k1} = 5$ kOe, $H_{k2} = 5$ kOe, $J_{ex} = 0.1$ erg/cm^2, referring to the CoFeB samples.[28] It can be seen that the dependence of acoustic and optical modes on the external magnetic field is very similar to the dispersion relation of the SAF with PMA.[28] It is worth noting that a frequency gap occurs when the magnetic field is about 3 kOe, which is due to the magnon–magnon coupling effect between acoustic and optical modes. The coupling strength is defined as $g = |f_{OM} - f_{AM}|_{min}/2$, and the coupling rate is defined as g/ω_0, where $\omega_0 = (f_{OM} + f_{AM})/2$ is the center frequency. The frequency gap is about 2.3 GHz. Therefore, the coupling strength is 1.15 GHz, and the coupling rate is 0.09. In this calculation, the exchange energy is relatively weak, which refers to the previous result in CoFeB/W/CoFeB structure.[28] Generally, the J_{ex} in magnetic heterojunction will be larger, which makes the experimentally measured frequency gap much larger.[29–32] Considering the FM and AFM coupling in the noncollinear magnetic structure, the coupling strength is given in Fig. 3(b). This indicates that the coupling strength increases almost linearly with the interlayer exchange energy J_{ex}. The slope of ferromagnetic coupling is slightly larger than that of antiferromagnetic coupling. In the following discussion, we mainly focus on the AFM coupling state. Magnon–magnon coupling primarily originates from the symmetry breaking of the magnetization configuration in the magnetic multilayers, and the interlayer exchange coupling has a significant impact on the coupling strength.

Furthermore, we study the influence of saturation magnetization on the coupling strength and rate. Figure 3(c) shows the coupling rate as a function of M_s, where $M_{s1} = M_{s2}$ and $J_{ex} = 0.1$ erg/cm^2. The range of M_s is from 100 emu/cm^3 to 1300 emu/cm^3, which has covered most current magnetic materials, including YIG ($\sim$ 140 emu/cm^3), $Ni_{80}Fe_{20}$ ($\sim$ 900 emu/cm^3) and $Co_{20}Fe_{60}B_{20}$ ($\sim$ 1300 emu/cm^3). It can be seen that the coupling rate g/ω_0 monotonically decreases with the increase of saturation magnetization, and the overall trend is similar to an inverse proportional function. A small saturation magnetization gives rise to a stronger coupling strength. This is partly because decreasing the saturation magnetization while maintaining a constant exchange energy density is equivalent to enhancing the RKKY interaction. Additionally, the disparity in saturation magnetization exacerbates the asymmetry between the two layers. When the M_s increases from 100 emu/cm^3 to 500 emu/cm^3, the coupling rate rapidly decreases from 0.42 to less than 0.2, correspondingly, the coupling strength changes from 9.3 GHz to 2.75 GHz. This result reveals that a lower M_s can lead to a stronger magnon–magnon coupling. Under the condition of the same total thickness, the M_s of magnetic multilayer with multiperiodic structure is lower than that of the monolayer film.[41] It means that there will be an ultra-strong magnon–magnon coupling in the noncollinear magnetic structure with multiperiodic magnetic films, which is consistent with the reported work.[36]

Figure 3(d) shows the coupling rate for the different saturation magnetizations in the range from 100 emu/cm^3 to

1300 emu/cm^3. When keeping the M_s of one FM layer constant and changing the M_s of the other FM layer, the coupling rate is similar to an inverse proportion function. Under the critical condition of ultra-strong coupling regime,[42–44] as shown by a dashed line, $g/\omega_0 = 0.1$. This indicates that the ultra-strong coupling state can be achieved when the two FM layers have hugely different saturation magnetization. Moreover, as M_{s1} and M_{s2} decrease, the coupling strength and rate gradually increase. When the M_s of the two FM layers is about 140 emu/cm^3, the coupling rate can reach around 0.38.

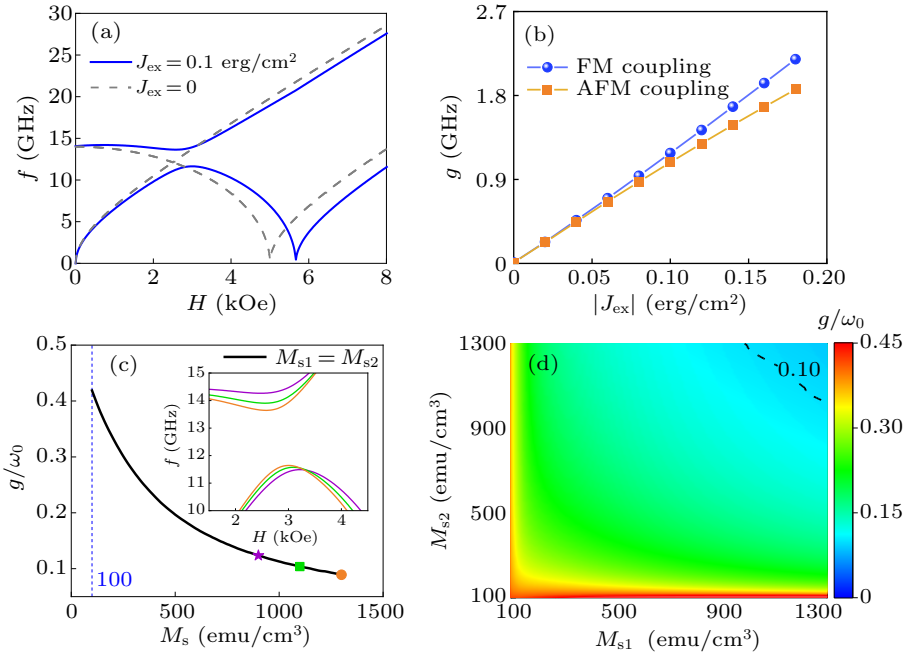


Fig. 3. The influence of M_s and J_{ex} on the coupling rate. (a) The frequency dispersion relation of the noncollinear magnetic structure, the black dashed line is the cross mode without magnon–magnon coupling. The inset shows the frequency dispersion in the range from 2.5 kOe to 3 kOe. (b) The relationship between magnon–magnon coupling strength and exchange energy density, the blue sphere means antiferromagnetic coupling and the orange square means ferromagnetic coupling. (c) The coupling rate as a function of saturation magnetization when the saturated magnetization $M_{s1} = M_{s2}$. The inset shows the variation of the frequency gap in the dispersion relation. The purple solid line (pentagram), green solid line (square), and orange solid line (circle) represent the saturation magnetization $M_s = 900$ emu/cm^3, 1100 emu/cm^3, and 1300 emu/cm^3, respectively. (d) Contour map of coupling rate. The dashed line ($g/\omega_0 = 0.1$) represents the boundary of ultra-strong coupling region.

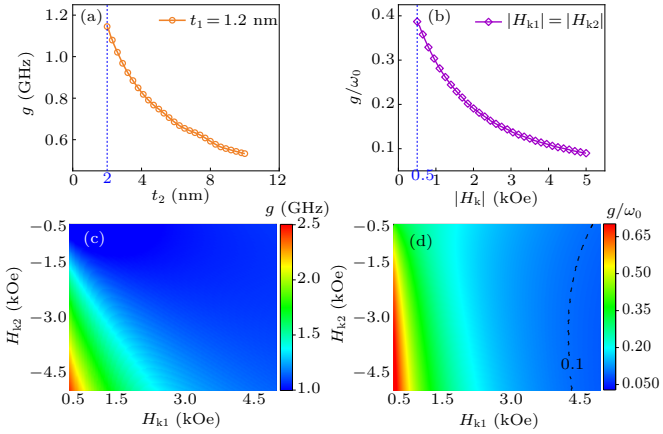


Fig. 4. The influence of H_k and t_2 on the coupling strength and coupling rate. (a) The relationship between magnon–magnon coupling strength and thickness of t_2 (IP-FM) when $t_1 = 1.2$ nm (PMA-FM). (b) The relationship between magnon–magnon coupling rate and anisotropy effective magnetic field when the absolute values of H_{k1} and H_{k2} are equal. The blue sphere means antiferromagnetic coupling and the orange square means ferromagnetic coupling. (c) Contour map of coupling strength. (d) Contour map of coupling rate. The dashed line ($g/\omega_0 = 0.1$) represents the boundary of ultra-strong coupling region.

Subsequently, we explore the influence of the perpendicular magnetic anisotropy and thickness of FM on magnon–magnon coupling. In the experiment, the ferromagnetic layer with perpendicular anisotropy cannot be too thick. Therefore, we only discuss the thickness variation relationship of IP-FM. Figure 4(a) shows the coupling strength as a function of the t_2 (IP-FM), as the thickness t_2 increases from 2 nm to 10 nm, the coupling strength decreases monotonically from 1.15 GHz to 0.53 GHz. The increase in thickness indicates a decrease in the volumetric energy density of the interlayer coupling, which leads to a reduction in the coupling strength. Figure 4(b) shows the coupling strength and rate as functions of the effective PMA (IP) field $H_{k1}(H_{k2})$, where $M_{s1} = M_{s2} = 1300$ emu/cm^3, and $J_{ex} = 0.1$ erg/cm^2. When H_k gradually increases from 0.5 kOe to 5 kOe, the coupling rate is reduced from 0.39 to 0.09. Figures 4(c) and 4(d) show the relationship between the coupling strength and the anisotropy field of the two ferromagnetic layers. Weak H_{k1} and strong H_{k2} lead to greater coupling strength and coupling rate. The coupling rate can reach approximately 0.7 when $H_{k1} = 500$ Oe and $H_{k2} = 5000$ Oe. A combination of low saturation magnetization and weak perpendicular magnetic anisotropy has the potential to achieve a higher coupling rate.

Then, we explore the influence of the wave vector on

magnon–magnon coupling. In Fig. 5, the orange line shows the coupling strength as a function of the wave vector in PMA-SAF. When the wave vector increases from 2 μm^{-1} to 20 μm^{-1}, the coupling strength linearly increases from 0.6 GHz to 1.2 GHz, and the parameters used in the calculation are taken from previous work.[28] This is because in the limit of $kt \ll 1$, the dynamic dipole field excited by the spin wave is proportional to the wave vector k. In the IP-SAF, the relationship between the coupling strength and the wave vector is also a similar linear relationship, which has been proven in experiments.[40] In noncollinear synthetic antiferromagnets, the dipole magnetic field experienced by PMA-FM is represented as $\boldsymbol{h}^{\rm PMA}_{\rm self-dip} + \boldsymbol{h}^{\rm IP}_{\rm mutual-dip}$, and the dipole magnetic field experienced by IP-FM is represented as $\boldsymbol{h}_{\rm dip,2} = \boldsymbol{h}^{\rm IP}_{\rm self-dip} + \boldsymbol{h}^{\rm PMA}_{\rm mutual-dip}$. In Fig. 5, the blue line shows the coupling strength as a function of the wave vector. When the $H_{\rm k1} = 5$ kOe and $H_{\rm k2} = 5$ kOe, the relationship between the coupling strength in T-SAF and the variation of the wave vector follows a similar linear pattern to that of PMA-SAF and IP-SAF. When the wave vector increases from 2 μm^{-1} to 20 μm^{-1}, the coupling strength linearly increases from 0.54 GHz to 1.12 GHz. Under the same exchange energy density and at $H_{\rm k1}$, as the wave vector increases gradually, the rate of growth of coupling strength in T-SAF is the same as that in PMA-SAF.

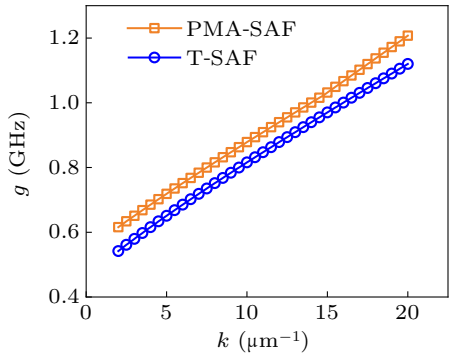


Fig. 5. The change in coupling strength with the wave vector. Orange squares represent PMA-SAF with a perpendicular anisotropic field $H_{\rm k1} = 4800$ Oe and $H_{\rm k2} = 2600$ Oe, exchange energy density $J_{\rm ex} = 0.1$ erg/cm^2, while blue circles indicate noncollinear synthetic antiferromagnets.

To gain insights into the magnon–magnon coupling, the time-domain results of magnetization dynamical response have been numerically calculated by using the same magnetic parameters as before. At the equilibrium state, a perturbing magnetic field is firstly applied and then removed, the magnetization then relaxes and the x-component of magnetization in two FM layers is recorded within 20 ns. The time-domain results are shown in the left of Fig. 6 when the external magnetic fields are 1000 Oe, 3000 Oe, 7000 Oe, respectively, and the corresponding frequency-domain results obtained through Fourier transform are shown in the right of Fig. 6. When the $H_{\rm ext} = 1000$ Oe, the $\boldsymbol{M}_1$ and $\boldsymbol{M}_2$ nearly form a T-shaped configuration. The m_{x1} and m_{x2} have different precession frequencies, and the amplitudes of m_{x1} and m_{x2} differ but remain essentially constant. The precession frequency of m_{x1} is composed of the superposition of AM and OM. When the $H_{\rm ext} = 7000$ Oe, the $\boldsymbol{M}_1$ and $\boldsymbol{M}_2$ are nearly parallel. The precession components of magnetization have higher resonance frequencies. When $H_{\rm ext} = 3000$ Oe, which corresponds to the precession at the frequency gap, the frequency of m_{x1} is also composed of the superposition of AM and OM. The amplitudes of m_{x1} and m_{x2} will undergo significant changes during precession. The maximum amplitude and minimum amplitude of the x-component of precession in two FM layers correspond to each other, in other words, the m_{x1} and m_{x2} alternately change in time domain. This indicates that the changes of amplitude during precession represent the exchange of energy and information between two resonance modes. This result demonstrates a clear understanding of the magnon–magnon coupling and facilitates the research of the hybrid quantum system based on magnon.

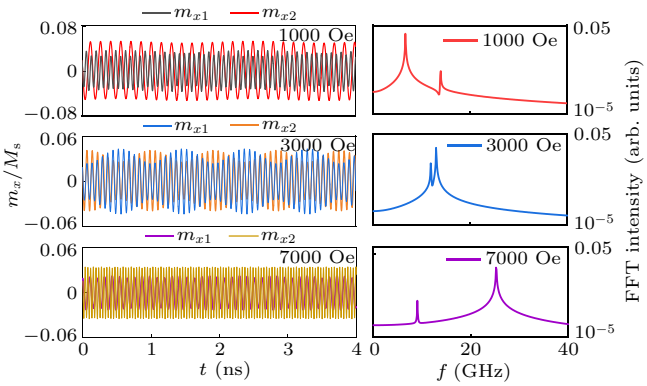


Fig. 6. Magnetization dynamical response in time domain (on the left) when the external magnetic field is 1000 Oe, 3000 Oe, 7000 Oe, respectively. The corresponding frequency-domain results (on the right) are obtained through Fourier transform. The images at the top show the precession information of a T-type configuration, the middle images correspond to the position of the frequency gap, namely, the magnon–magnon coupling, and the bottom images show the precession information when the magnetizations in two FM layers are parallel.

In summary, we have studied the magnon–magnon coupling in a noncollinear SAF through the theoretical and numerical methods. The coupling strength is determined by the physical parameters, including the saturation magnetizations of two FM layers, perpendicular magnetic anisotropy, interlayer exchange interaction, and spin wave vector. The coupling strength has a linear relationship with the interlayer exchange energy. The saturation magnetization of the FM layer has a remarkable influence on the coupling strength, and the ultra-strong magnon–magnon coupling can be achieved at the condition of lower saturation magnetization. Moreover, we find that the magnetization precession at the position of frequency gap represents the exchange of energy and information between two resonance modes. This work provides a helpful

insight into the magnon–magnon coupling in the noncollinear SAF.

Acknowledgements

Project supported by the National Natural Science Foundation of China (Grant No. 52201290), the Natural Science Foundation of Gansu Province (Grant No. 24JRRA402), and the 9th Research Institute of China Electronics Technology Group Corporation's open projects (Grant No. 2024SK-001-4).

References

[1] Lenk B, Ulrichs H, Garbs F and Münzenberg M 2011 *Phys. Rep.* **507** 107
[2] Holstein T and Primakoff H 1940 *Phys. Rev.* **58** 1098
[3] Dyson F J 1956 *Phys. Rev.* **102** 1217
[4] Kruglyak V V, Demokritov S O and Grundler D 2010 *J. Phys. D: Appl. Phys.* **43** 264001
[5] Serga A A, Chumak A V and Hillebrands B 2010 *J. Phys. D: Appl. Phys.* **43** 264002
[6] F Bloch 1930 *Z. Physik* **61** 206
[7] Hertel R, Wulfhekel W and Kirschner J 2004 *Phys. Rev. Lett.* **93** 257202
[8] Lee K S, Han D S and Kim S K 2009 *Phys. Rev. Lett.* **102** 127202
[9] Schneider T, Serga A A, Leven B, Hillebrands B, Stamps R L and Kostylev M P 2008 *Appl. Phys. Lett.* **92** 022505
[10] Kostylev M P, Serga A A, Schneider T, Leven B and Hillebrands B 2005 *Appl. Phys. Lett.* **87** 15350
[11] Rameshti B Z, Kusminskiy S V, Haigh J A, Usami K, Lachance-Quirion D, Nakamura Y, Hu C M, Tang H X, Bauer G E W and Blanter Y M 2022 *Phys. Rep.* **979** 1
[12] Tabuchi Y, Ishino S, Noguchi A, Ishikawa T, Yamazaki R, Usami K and Nakamura Y 2015 *Science* **349** 405
[13] Huebl H, Zollitsch C W, Lotze J, Hocke F, Greifenstein M, Marx A, Gross R and Goennenwein S T B 2013 *Phys. Rev. Lett.* **111** 127003
[14] Goryachev M, Farr W G, Creedon D L, Fan Y, Kostylev M and Tobar M E 2014 *Phys. Rev. Appl.* **2** 054002
[15] Lachance-Quirion D, Tabuchi Y, Gloppe A, Usami K and Nakamura Y 2019 *Appl. Phys. Express* **12** 070101
[16] Tabuchi Y, Ishino S, Ishikawa T, Yamazaki R, Usami K and Nakamura Y 2014 *Phys. Rev. Lett.* **113** 083603
[17] Liensberger L, Kamra A, Maier-Flaig H, Geprägs S, Erb A, Goennenwein S T B, Gross R, Belzig W, Huebl H and Weiler M 2019 *Phys. Rev. Lett.* **123** 117204
[18] Chen J, Yu T, Liu C, Liu T, Madami M, Shen K, Zhang J, Tu S, Alam M S, Xia K, Wu M, Gubbiotti G, Blanter Y M, Bauer G W and Yu H 2019 *Phys. Rev. B* **100** 104427
[19] Chen J, Liu C, Liu T, Xiao Y, Xia K, Bauer G E W, Wu M and Yu H 2018 *Phys. Rev. Lett.* **120** 217202
[20] Adhikari K, Choudhury S, Barman S, Otani Y and Barman A 2021 *Nanotechnology* **32** 395706
[21] Xiong Y, Li Y, Hammami M, Bidthanapally R, Sklenar J, Zhang X, Qu H, Srinivasan G, Pearson J, Hoffmann A, Novosad V and Zhang W 2020 *Sci. Rep.* **10** 12548
[22] MacNeill D, Hou J T, Klein D R, Zhang P, Jarillo-Herrero P and Liu L 2019 *Phys. Rev. Lett.* **123** 047204
[23] Li M, Lu J and He W 2021 *Phys. Rev. B* **103** 064429
[24] Wiese N, Dimopoulos T, Rührig M, Wecker J, Brückl H and Reiss G 2004 *Appl. Phys. Lett.* **85** 2020
[25] Waring H J, Li Y, Moutafis C, Vera-Marun I J and Thomson T 2021 *Phys. Rev. B* **104** 014419
[26] Belmeguenai M, Martin T, Woltersdorf G, Bayreuther G, Baltz V, Suszka A K and Hickey B J 2008 *J. Phys.: Condens. Matter* **20** 345206
[27] Martin T, Belmeguenai M, Maier M, Perzlmaier K and Bayreuther G 2007 *J. Appl. Phys.* **101** 09C101
[28] Zhang T, Li C, Zhao Q, Li Z, Wang Q, Yu G, Han X, Chai G, Zhang S, Liu Q, Wang J, Wei J 2024 *Phys. Rev. B* **109** 054406
[29] Sud A, Yamamoto K, Suzuki K Z, Mizukami S and Kurebayashi H 2023 *Phys. Rev. B* **108** 104407
[30] Dai C and Ma F 2021 *Appl. Phys. Lett.* **118** 112405
[31] Sud A, Zollitsch C W, Kamimaki A, Dion T, Khan S, Iihama S, Mizukami S and Kurebayashi H 2020 *Phys. Rev. B* **102** 100403
[32] Hu B and He W 2023 *J. Magn. Magn. Mater.* **565** 170283
[33] Lu S, Meng D, Khan A, Wang Z, Chen S and Liang S 2024 *Chin. Phys. B* **33** 107501
[34] Wang X R 2022 *Chin. Phys. Lett.* **39** 027301
[35] Zhu M, Dong J, Li X, Zheng F, Zhou Y, Wu K and Zhang J 2024 *Chin. Phys. Lett.* **41** 047502
[36] Wang Y, Zhang Y, Li C, Wei J, He B, Xu H, Xia J, Luo X, Li J, Dong J, He W, Yan Zh, Yang W, Ma F, Chai G, Yan P, Wan C, Han X and Yu G 2024 *Nat. Commun.* **15** 2077
[37] Nortemann F C, Stamps R L and Camley R E 1993 *Phys. Rev. B* **47** 11910
[38] Stamps R L 1994 *Phys. Rev. B* **49** 339
[39] Skarsvåg H, Kapelrud A and Brataas A 2014 *Phys. Rev. B* **90** 094418
[40] Shiota Y, Taniguchi T, Ishibashi M, Moriyama T and Ono T 2020 *Phys. Rev. Lett.* **125** 017203
[41] Mendisch S, Žiemys G, Ahrens V, Papp Á and Becherer M 2019 *J. Magn. Magn. Mater.* **485** 345
[42] Niemczyk T, Deppe F, Huebl H, Menzel E P, Hocke F, Schwarz M J, Garcia-Ripoll J J, Zueco D, Hümmer T, Solano E, Marx A and Gross R 2010 *Nat. Phys.* **6** 772
[43] Frisk Kockum A, Miranowicz A, De Liberato S, Savasta S and Nori F 2019 *Nat. Rev. Phys.* **1** 19
[44] Ishibashi M, Shiota Y, Li T, Funada S, Moriyama T and Ono T 2020 *Sci. Adv.* **6** eaaz6931